Frequency-based analysis of active laser thermography for spot weld quality assessment

Original
Frequency-based analysis of active laser thermography for spot weld quality assessment / Santoro, L., Razza, V., De Maddis, M.. - In: INTERNATIONAL JOURNAL, ADVANCED MANUFACTURING TECHNOLOGY. - ISSN 0268-3768. - (2024). [10.1007/s00170-023-12845-5]

Publisher:
Springer Nature

Published
DOI:10.1007/s00170-023-12845-5

The International Journal of Advanced Manufacturing Technology (2024) 130:3017–3029
https://doi.org/10.1007/s00170-023-12845-5

ORIGINAL ARTICLE

Frequency-based analysis of active laser thermography for spot weld quality assessment

Luca Santoro[1] · **Valentino Razza**[2] · **Manuela De Maddis**[2]

Received: 27 June 2023 / Accepted: 6 December 2023 / Published online: 27 December 2023

Abstract

Resistance spot welding (RSW) is a widely employed technique for joining metallic components in different sectors of various industries. However, the quality of the weld joints has a significant influence on the mechanical properties of the joints. This paper presents an innovative non-destructive inspection technology based on active thermography for assessing the welding quality as a function of the peak load. By employing a frequency-modulated laser heat source, we analyze the thermal signal that traverses the weld joint section. Then, we establish a correlation between welding quality and the information derived from spot size and internal uniformity analysis. Furthermore, the proposed methodology shows potential for in-line testing of resistance spot welding, offering easy automation and enabling the classification of spot-welded joints.

Keywords Resistance spot weld · NDT · Thermography · Frequency response

1 Introduction

Resistance spot welding (RSW) is a widely employed technique for joining metallic components in different sectors due to its efficiency and cost-effectiveness. The mechanical properties of spot welds play a crucial role in determining joint structural integrity and overall performance. Traditionally, weld quality is monitored through destructive testing, such as peel and chisel tests, and the measures of weld attributes, such as the shape and size of the weld nugget. These analyses are the only reliable methods to measure the welding quality accurately.

Studies show some relations between the welding process parameters and the joint quality. For example, in [44], the authors have studied the effect of electrode pressure on nugget size, showing how the nugget size and metallurgical composition influence the tensile-shear strength of the joint. In [25], the influences of the microstructural changes, when welded by RSW, and nugget dimension on the DP600 mechanical properties are shown. Under certain conditions, the so-called *expulsion* occurs. In [42] and [43], a deep study is presented, where the authors demonstrate how this influences the mechanical properties of the joint. Indeed, in [56], a review of resistance spot weld quality assessment techniques is presented, showing how the nugget diameter is one of the main indicators of weld quality, but it cannot give an ultimate criterion for mechanical quality assessment. The standards AWS D8.1M:2013 [2] and AWS D8.9M:2022 [4] indicate several inspection methods to define the weld quality. Not all methods need to be applied. The most appropriate to define the quality of the specific application must be determined by an agreement between the customer and supplier. Standard destructive inspections used in industry are aimed at ensuring the presence of a minimum nugget diameter to ensure minimum load resistance and the absence of expulsion of a portion of molten metal from the nugget, resulting in thinning of the weld and the presence of voids in the nugget so resulting in significant degradation of weld strength. Further details are given in [23].

Destructive sample testing is needed to monitor the weld quality and process stability over time. This type of control

✉ Luca Santoro
luca.santoro@polito.it

Valentino Razza
valentino.razza@polito.it

Manuela De Maddis
manuela.demaddis@polito.it

[1] Dipartimento di Ingegneria Meccanica e Aerospaziale - Politecnico di Torino, Corso Duca degli Abruzzi 24, Torino 10129, Italy

[2] Dipartimento di Ingegneria Gestionale e della Produzione - Politecnico di Torino, Corso Duca degli Abruzzi 24, Torino 10129, Italy

leads to losing a percentage of the assembled parts through an expensive and time-consuming procedure. Moreover, being performed only on a sample basis does not allow many defective welds to be identified, so manufacturers often require more welds to be performed than required [30].

Therefore, much attention is devoted to developing non-destructive testing (NDT) techniques to accurately assess the weld quality, which may save the cost of scrap parts and allow 100% accuracy in the inspection.

Identifying a *good weld* joint through non-destructive analyses is of interest in both scientific and industrial communities. Different NDT techniques based on radiographic, ultrasonic, or acoustic inspection have been developed but with some limitations that result in being time-consuming and not cost-effective, affected by human factors and environmental conditions [12, 33, 36, 39, 60]. Over the years, many attempts have been made to correlate the mechanical resistance of a spot weld with its real feature and a non-destructive evaluated feature. Non-destructive testing of spot weld usually does not allow for an accurate evaluation of the weld goodness. In fact, industries usually add 20% of the welds to assess the low accuracy of non-destructive testing of the RSWs [39, 59]. In technical literature, several researchers focus on thermographic testing and monitoring methods. Thermography is a non-contact technique used to obtain thermal maps of the surface of a component during an observation period (see, e.g., [5, 6, 8, 11, 17–20, 22, 26, 31, 32, 35, 37, 41, 45–49, 51–54, 57, 61]).

A promising approach within the thermographic testing technology is the *active*, or *stimulated*, thermography. In active thermography, the component to be analyzed is thermally excited by an external heat source to characterize thermal properties and/or detect flaws during the observation period. Experimental results show that the thermal response of a volume of a component with a defect is different than in sound regions(see, e.g., [11, 15, 31, 46]). Active thermography adapts well to the investigation of welding microstructure and defect detection, and it is widely applied for composites and laminates (see, e.g., [6, 21, 41]). Thermal stimulation can be classified into two categories: photo-thermal stimulation, which introduces heat through the surface, and volumetric stimulation, where the heat is produced in the bulk of the material by dissipative phenomena. Ultrasound stimulation achieves some promising results within active thermography, where cracks are found in aluminum structures [18], as well as in dissimilar metal welds [38]. Another volumetric stimulation is electromagnetic induction. In [9], an induction system is used to heat a stainless steel weld. Yuan et al. [58] propose induction thermography for condition monitoring of overlay welded components under multi-degradation; one of the main advantages of this technique is that, with proper signal processing, it can give a visual indication of anomalies. In [16], the authors combine laser, induction, and heat-gun stimulation to detect defects in nickel superalloy welds.

Active thermography is gaining interest in the scientific community, especially for NDT. The authors in [7] detect superficial cracks through laser stimulation. A similar approach is proposed in [29], where the algorithm efficiency is improved through a post-processing analysis based on the second temporal derivative. In [50], active thermography is used to assess the spot-welded joint quality through statistical results of average spot behaviors. The combination of laser and lamp stimulation is used to evaluate Cu solder connections ([32]). In general, active thermography is not used only for defect detection but can also give important information about the welded area. In [13], the authors use laser stimulation to measure the welded area in resistance projection welding, while microstructural properties of heat-treated steel are detected in [14].

As regards the application of active thermography technique as NDT of resistance spot weld, [50] present a temperature increase-based approach. The methodology uses a graphite paint coat to assess the emissivity, but any consideration about the mechanical resistance of the welds is done. In [26], a qualitative approach to thermographic testing of RSW is presented, where the thermal response of different tested joints is analyzed for both reflection and transmission configuration. The authors present different thermal response curves for different welding currents, but no estimation of nugget size is given, and no correlation with mechanical properties is presented. A similar approach is proposed in [47], where the authors try to estimate the nugget size in a reflection configuration. Still, the estimation suffers errors arising from the weld spot surface irregularities.

The present work proposes a technique based on active thermography for evaluating weld quality in relation to peak load. The thermal signal passing through the weld section is analyzed using a frequency-modulated laser heat source. To reduce the uncertainties due to measurement and emissivity coefficients, the thermal data is evaluated in the frequency domain, represented in terms of magnitude and phase of a complex numerical function in frame space. By evaluating the signal magnitude, information on the size of the weld spot is extracted, while the phase provides information on the uniformity of the spot. A correlation was found between the estimated spot size and internal uniformity and weld quality.

The remainder of the paper is organized as follows. Section 2 presents the analytical background of the thermal phase analysis. The RWS process, active thermography setup, and data analysis are defined in Sect. 3. Section 4 presents the results of the innovative NDT, together with the relationship between the estimated features and the UTS and the resulting weld quality classification. Finally, conclusions and future work end the paper.

2 Analytical background

The idea at the basis of this work is that both thickness and thermal diffusivity influence the through-plane measured thermal phase. In this section, we introduce the mathematical model that describes the thermal behavior of a single slab subjected to an external thermal source. The analytical background reported here is based on the results from [10].

A laser beam exciting a slab of thickness ℓ is considered. For the sake of simplicity, the slab is opaque with an infinite surface. The laser beam, having power P_0, is characterized by a Gaussian profile at $1/e^2$ with radius a. Thus, the laser power transferred to the sample is given by

$$P(r) = \eta \frac{P_0}{\pi a^2} e^{-2r^2/a^2}, \tag{1}$$

where η is the power fraction absorbed, and r is the distance from the center of the laser spot. The slab is considered surrounded by air and the laser beam is modulated at frequency f (i.e., $\omega = 2\pi f$). Only the oscillation component of the temperature $T(r, z)$ is studied. To distinguish the heated and rear surfaces, subscripts $e1$ and $e2$, respectively, are used, while the sample is identified by the subscript s (see Fig. 1). Due to the cylindrical geometry, the oscillating component of the temperatures of each medium is defined through the Hankel transforms

$$T_{e1}(r, z) = \int_0^\infty \delta J_0(\delta r) K_1 e^{\beta_e z} d\delta, \tag{2a}$$

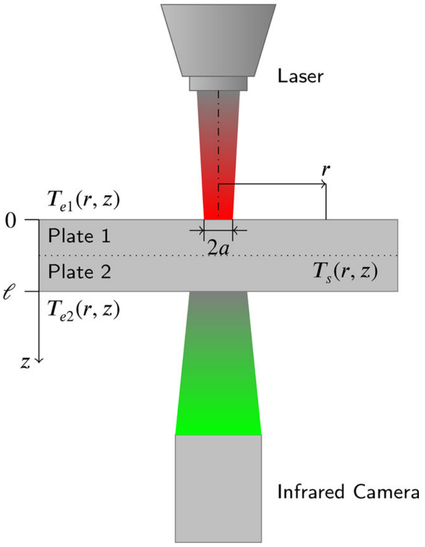

Fig. 1 Cross-section of the experimental setup and the reference system. The laser excites one side of the specimen, while the infrared camera acquires the rear sample temperature. The two plates joined together are considered a unique slab for the model in Sect. 2

$$T_s(r, z) = \int_0^\infty \delta J_0(\delta r) \left[K_2 e^{-\beta_s z} + K_3 e^{\beta_s z}\right] d\delta, \tag{2b}$$

$$T_{e2}(r, z) = \int_0^\infty \delta J_0(\delta r) K_4 e^{\beta_e(-z+\ell)} d\delta, \tag{2c}$$

where J_0 is the Bessel function of the 0-th order, δ is the Hankel variable, $\beta_x^2 = \delta^2 + i\omega/D_x$, $x = \{e, s\}$, and $i = \sqrt{-1}$. D_e and D_s are the air and sample diffusion coefficients, respectively, and $K_i, i = 1, \ldots, 4$ are constant coefficients determined from the boundary conditions that guarantee the temperature continuity along the slab boundaries

$$T_{e1}(r, 0) = T_s(r, 0) \tag{3a}$$

$$T_{e2}(r, \ell) = T_s(r, \ell), \tag{3b}$$

and the heat transfer equilibrium along the surfaces (by convection and radiation), i.e.,

$$\begin{aligned} -K_s \frac{\partial T_s}{\partial z}\bigg|_{z=0} &= -K_e \frac{\partial T_{e1}}{\partial z}\bigg|_{z=0} + hT_s|_{z=0} \\ &\quad - \eta \frac{P_0}{2\pi} \int_0^\infty \delta J_0(\delta r) e^{(\delta a)^2/8} d\delta, \end{aligned} \tag{4a}$$

$$-K_s \frac{\partial T_s}{\partial z}\bigg|_{z=\ell} = -K_e \frac{\partial T_{e2}}{\partial z}\bigg|_{z=\ell} + hT_s|_{z=\ell}, \tag{4b}$$

where K_e and K_s are the air and sample thermal conductivity, respectively. h is the heat transfer coefficient, which considers the combined effect of convection and radiation on the outer surfaces. By combining Eqs. 2–4, the overall oscillating component slab temperature equation is

$$\begin{aligned} &T_s(r, z) = \\ &\frac{\eta P_0}{4\pi} \int_0^\infty \delta J_0(\delta r) e^{-(\delta a)^2/8} \frac{A e^{-\beta_s(z-\ell)} + B e^{\beta_s(z-\ell)}}{A^2 e^{\beta_s \ell} - B^2 e^{-\beta_s \ell}} d\delta, \end{aligned} \tag{5}$$

where $A = K_s\beta_s + K_g\beta_g + h$ and $B = K_s\beta_s - K_g\beta_g - h$.

An interested reader may refer to [10] for further details on the slab temperature model.

In our application, the sample is made of steel, characterized by thermal conductivity $K_s \gg K_e$ (for air, the standard value at ambient temperature $K_e \approx 0.025\,\mathrm{W\,m^{-1}K^{-1}}$). Moreover, for non-low frequency f, i.e., $f \geq 1\mathrm{Hz}$, $K_e\beta_e \ll K_s\beta_s$, and $h \ll K_s\beta_s$, and Eq. 5 can be rewritten as

$$\begin{aligned} &T_s(r, z) \approx \\ &\frac{\eta P_0}{4\pi K_s} \int_0^\infty \delta J_0(\delta r) \frac{e^{-(\delta a)^2/8}}{\beta_s} \frac{e^{-\beta_s(z-\ell)} + e^{\beta_s(z-\ell)}}{e^{\beta_s \ell} - e^{-\beta_s \ell}} d\delta. \end{aligned} \tag{6}$$

We are interested in evaluating the rear sample temperature acquired by an infrared camera. From Eq. 6, we get

$$T_s(r,\ell) \approx \frac{\eta P_0}{2\pi K_s}\int_0^\infty \frac{\delta J_0(\delta r)}{\beta_s}\frac{e^{-(\delta a)^2/8}}{e^{\beta_s \ell} - e^{-\beta_s \ell}}d\delta. \tag{7}$$

This formula has no analytical solution. However, the laser power to the rear temperature phase delay is evaluated through numerical simulation. From [28], the phase delay is given by

$$\phi = -\ell/\lambda, \tag{8}$$

where $\lambda = \sqrt{2D_s/\omega}$ is the thermal diffusion length. Moreover, Eq. 8 does not account for nonlinearities due to small thermal diffusivity coefficient or low laser modulation frequency (see, e.g., [10]). From the authors' experience, the laser power must be set accordingly to have at least 10 °C temperature increase from ambient temperature to have reliable data.

3 Materials and methods

3.1 RSW process

The spot welds have been obtained using an industrial medium frequency direct current (MFDC) RSW machine (see Fig. 2).

The experimental tests are conducted on coupons made on DP590 galvanized steel sheets, commonly used to produce car body parts, 1 mm thick, using Cu-Cr-Zr electrodes with a truncated cone shape with a nominal contact diameter of 6 mm. During the welding procedure, the electrodes have been cooled through a water flow of about 4 L min^{-1}. The welding procedure and the face diameter of the electrodes have been chosen based on the recommendations from [4]. Different kinds of spot welds have been generated by varying the machine parameters to achieve three different cases:

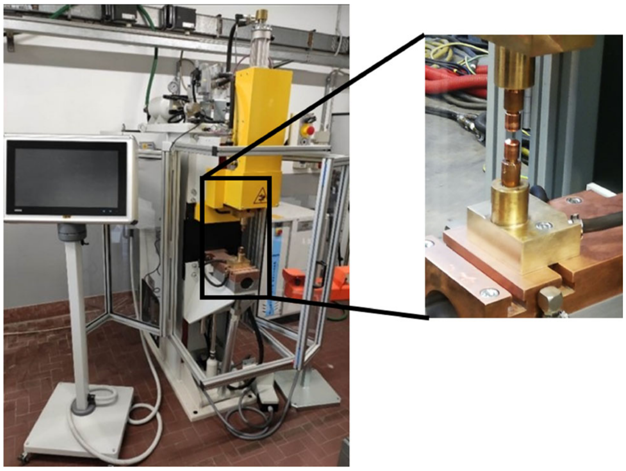

Fig. 2 Resistance spot weld experimental setup

- Undersized weld: conditions that lead to "bad" spot welds due to a low current value and thus the presence of an undersized nugget
- Acceptable weld: a condition leading to "good" spot welds obtained with the optimized process parameters (within limits defined by the standard)
- Expulsion limit: a condition leading to "bad" spot welds due to high current and the presence of spatter due to an excessive current level and thus the presence of spatter

A pilot experiment has been conducted to define the process parameters for the three different weld sizes. The optimal process parameter has been chosen to obtain the best mechanical characteristics, no-splash, and pull-out mode of fracture, leading to a nugget size about four times the square root of the thickness of the sheet, larger than the required size according to [4], and minimum tensile-shear strength (TSS) required by the standard higher than 5 kN. The relative process parameters are set according to standard [4] and summarized in Table 1. The squeeze and hold times have been kept to 100 ms and 300 ms, respectively. Thus, the electrodes were released from the specimen 300 ms after the weld current is switched off.

The quality of a weld is usually expressed by some features, either from a direct visual inspection or measured through destructive tests. Commonly used weld attributes are nugget/ZTA, penetration, indentation/cracks (surface and internal), porosity/voids, sheet separation, and surface appearance. Among these attributes, weld size, evaluated as the nugget width, is the most frequently measured and meaningful in determining weld strength. However, in some contexts, nugget size alone, which determines the area of fusion and its load-bearing capability, is insufficient in describing a weld quality as it does not necessarily imply the structural integrity of the weld. For example, a reduction in tensile and shear strength may be due to an increase in current, which leads to greater heat input and, thus, a reduction in the time required to reach melting temperature. The consequence is a larger nugget size, leading to sensitive variation in nugget diameter, reduced thickness, deeper electrode

Table 1 Process parameter

No.	1	2	3
Electrode pressure (kN)	3	3	3
Welding time (ms)	300	300	300
Welding current (kA)	7	8.5	13

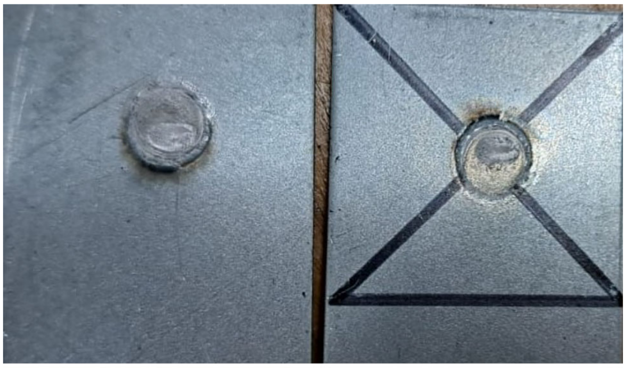

(a) Interfacial mode.

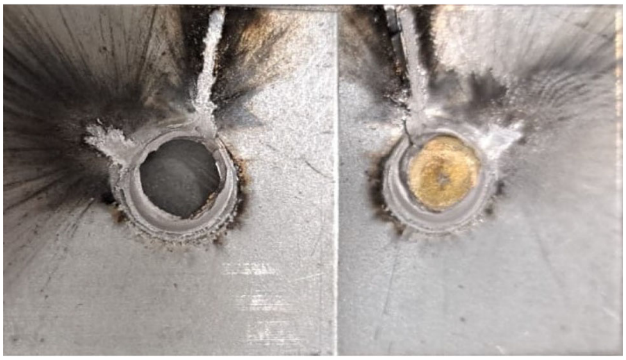

(b) Pullout mode and spatters.

Fig. 3 Failure modes

marks, and larger deformations. Thus, other weld features, e.g., microstructural composition [25, 44] and hardness or presence of expulsion [43], may complement the nugget size and provide useful information on the degree of adhesion.

3.2 Inspection

Weld performance is evaluated in terms of tensile-shear strength (peak load) and failure mode, e.g., interfacial fracture (in Fig. 3a) and pull-out (in Fig. 3b) [3].

The peak load in the tensile-shear test has been evaluated through the maximum load the weld can withstand. Using a standard testing machine, the shear tension samples have been carried out with a 10 mm min^{-1} crosshead speed.

Table 2 Active thermography set-up parameters

Modulation frequency	0.5 Hz
N° of pulses	25
Laser power	50 W
Laser spot diamater	10 mm
Power density	0.64 W mm
Acquisition frame rate	100 Hz
IR range	0–90 °C

The shear tension tests are 30 mm × 100 mm, with an overlapping area of 30 mm, according to JIS X 3136 (Japanese Standard Association 2018).

Additionally, since the best parameter that describes the mechanical properties is the nugget (see, e.g., [56]), metallurgical analysis has been done to measure nugget geometry and detect internal porosities. The specimens are prepared by being cut in the half of the spot weld, mounted, polished with 1µm diamond past, and then etched with Nital 1%. Finally, macrography analysis of the welds is carried out employing a Zeiss Axio Observer microscope. In the resulting cross-section of the weld, it is possible to make several measurements defined as nugget and heat-affected zone (HAZ) dimensions, such as diameter and penetration and the depth of the electrode indentation [24].

The experimental active thermography equipment (Fig. 4) comprises a thermal camera, a laser excitation source, and a PC control unit. The IR thermal camera is a cooled InSb FLIR A6750sc, having a sensitivity lower than 20 mK, equipped with a lens characterized by 50 mm focal length and a 3-5µm spectral range. The laser source can generate a maximum power of 50 W concentrated in a circular spot 10 mm in diameter. The experimental configuration is set in transmission mode as shown in Fig. 1, and the setup parameters are presented in Table 2. A similar approach used in the *Lock-In thermography* [34, 40, 55] is used, where a repeated step pulse modulated at a specific modulation frequency,

Fig. 4 Active thermography experimental setup

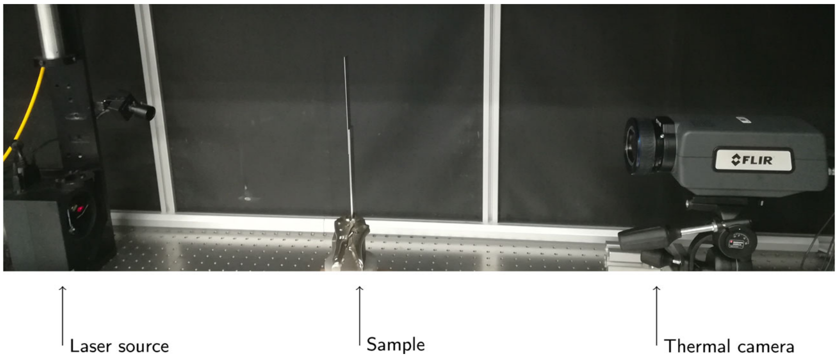

i.e., the *lock-in frequency*, is applied to the specimen. This technique allows for more advanced signal processing techniques, resulting in more consistent and accurate results.

The experiments have been run at 26.0 °C room temperature, relative humidity 30%, and a distance between the laser source and the target of 530 mm. With this setup, the parameters regarding the field of view are HFOV=200 mm, VFOV=160 mm, and an IFOV=0.32 mm.

3.3 Post-processing

The infrared camera provides the thermal behavior of the excited spot (see Fig. 5). The data is organized in a 3D matrix $T_k^{(r,c)}$, where $k = 0, \ldots, N-1$ are the discrete-time samples $t = kT_s$, $T_s = 1/f_r$ is the camera sampling time, $r = 1, \ldots, H$ and $c = 1, \ldots, W$ are row and column indexes, respectively, and the frame size is $H \times W$ pixels.

By selecting one pixel (r, c) (e.g., the red pixel in Fig. 5), we get the one-dimensional vector $T_k^{(r,c)}$, which contains the thermal behavior of the selected point. For the sake of simplicity in the notation, we omit the pixel index (r, c) in the latter unless it is necessary for the algorithm, i.e., $T_k = T_k^{(r,c)}$. Figure 6 shows a time-based profile of T_k for a single pixel (r, c) acquired during an experiment, where the specimen was thermally excited through a pulsed laser input acting at 2 Hz. The temperature signal is affected by uncertainties. In particular, the acquired temperature is affected by additive noise due to the thermal camera sensor. In Fig. 6, we see the measurement noise at the beginning of the temperature signal T_k before switching on the laser. The noise is present throughout the whole sequence. Denoising T_k can be done by applying low-pass filters or single value decomposition (SVD) based techniques (see, e.g., [27]). However, in general, the denoising techniques intrinsically modify the original signal, and not all noise components can be removed.

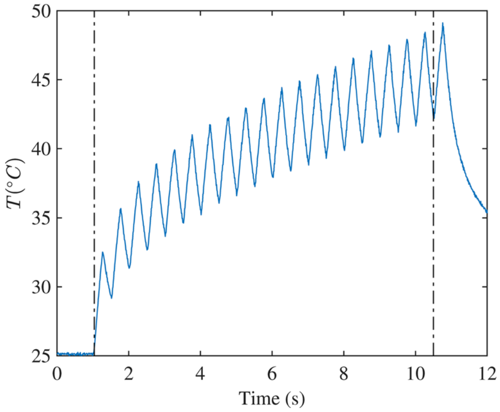

Fig. 6 Example of temperature signal acquired from the thermal camera for a single pixel. Dash-dotted lines represent the time of the first and the last temperature rise profile due to the laser impulses

Fig. 5 Video data structure. $T_k^{r,c}$ represents the temperature of the pixel (r, c) acquired at time k

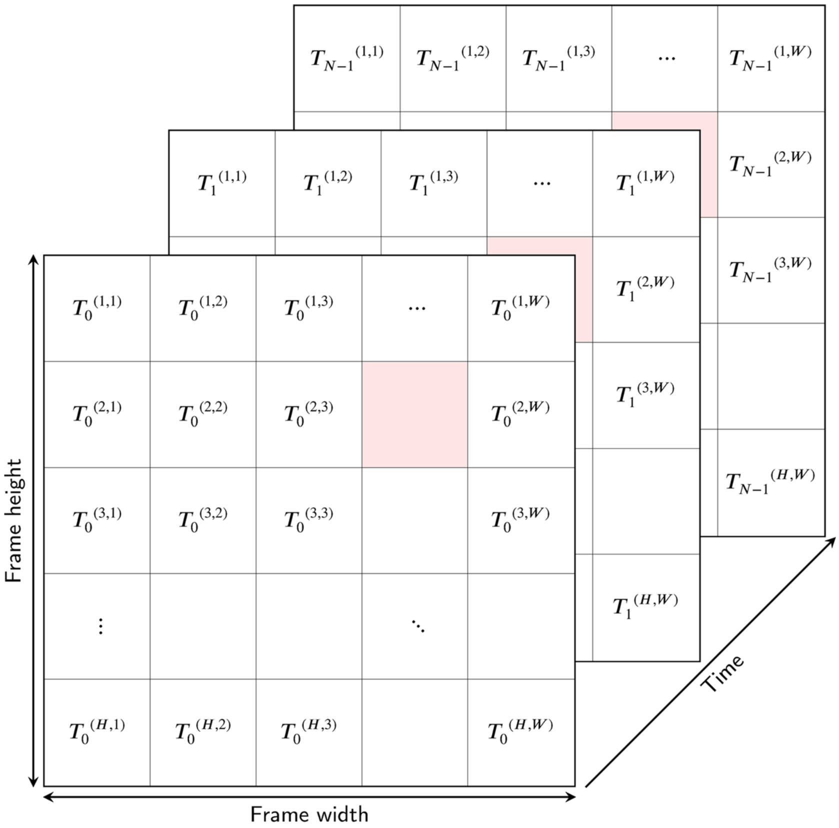

Moreover, even considering T_k as noise-free, the absolute temperature value from the thermal camera depends on the emissivity coefficient ϵ, which is not uniform along the surface. Figure 7 shows the first temperature frame $T_1^{(r,c)}$ acquired from the thermal camera. The expected temperature should be uniform along the surface since no external heat sources are acting on the sample. However, the shape of the spot weld is highlighted by large temperature variation along the surface, ranging from 25 to 28 °C. This problem is due to the emissivity coefficient uncertain value along the surface, which depends not only on the material but also on shape and color. Thus, the superficial defects, e.g., the marks due to the welding process, prevent precise temperature measurement. However, measurement noise and emissivity coefficient uncertainty affect the absolute value of the acquired temperature, not the overall signal behavior (e.g., temperature rising and decreasing, oscillations frequency). Thus, accurate information can be obtained through the frequency analysis of the signals $T_k^{(r,c)}$.

The *Fourier transform* is one of the most used operators in signal analysis. Due to the original formulation, the Fourier transform requires a continuous-time signal to be processed. However, due to the intrinsic sampling from the thermal camera at a given frame rate, only the sampled signal sequence T_k is known for each pixel frame. Thus, the *discrete Fourier transform* (DFT) is used to convert a uniformly sampled sequence of length N into an equally spaced sequence of the Fourier transform. Given the sequence T_k, $k = 0, \ldots, N-1$, the DFT is defined as

$$\tilde{T}_n = \sum_{k=0}^{N-1} T_k \, e^{-\frac{i2\pi nk}{N}} \in \mathbb{C}, \ \forall n = 0, \ldots, N-1. \tag{9}$$

The output is a sequence of N complex numbers denoted by $\tilde{T}_n$, whose amplitude and phase are related to sinusoidal signals at frequency $f = n \ f_r/N$. The original signal T_k can be retrieved through the linear combination of all the N sinusoids defined by $\tilde{T}_n$.

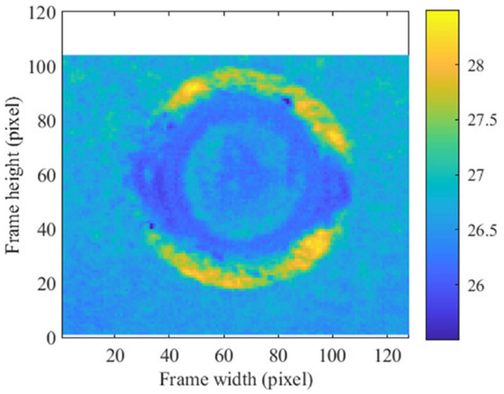

Fig. 7 Initial temperature frame acquired from the thermal camera. The colors define the temperature, in celsius, according to the palette on the right

Remark 1 It is worth noting that $\tilde{T}_n = \tilde{T}^*_{N-n}$ since the sequence $T_k \in \mathbb{R}$, where $\tilde{T}^*_n$ is the complex conjugated value of $\tilde{T}_n$. Thus, thanks to this symmetry, the analysis of $\tilde{T}_n$ is limited to $n = 0, \ldots, \lceil (N-1)/2 \rceil$, where $\lceil x \rceil$ is the rounding to the next integer. An interested reader finds further details about the DFT properties in [1].

To evaluate the size of the welded region, we observe that the steel sheets propagate the thermal wave through the welded spot only. In fact, outside the welded region, a thin air layer is intrinsically present within the metal sheets that prevent direct heat propagation from one side to the other of the specimen. Thus, within the welded region, a heat source, acting at a given frequency f_ℓ on one side of the specimen, leads to a component in the module of $\tilde{T}_n$ at f_ℓ above to the noise level.

It is worth noting that the uncertainty on the emissivity coefficient leads to an incorrect temperature conversion from the radiance value, i.e., through the Stefan-Boltzmann Law $R = \epsilon T^4$. An incorrect ϵ value leads to a vertical stretch of the temperature signal (e.g., the one depicted in Fig. 6). However, the oscillations due to the pulsed laser heat source will be present independently by the ϵ value. From Eq. 9,

$$\tilde{T}_0 = \sum_{k=0}^{N-1} T_k, \tag{10}$$

i.e., $\tilde{T}$ evaluated at 0 is a real number given by the integral of the temperature along the time. The DTF signal module $|\tilde{T}|$ is normalized by $\tilde{T}_0$, i.e.,

$$\hat{T}_n = \frac{\left|\tilde{T}_n\right|}{\tilde{T}_0}, \ n = 1, \ldots, \lceil (N-1)/2 \rceil. \tag{11}$$

Only $\hat{T}_{n_\ell}$ for $n_\ell = N f_\ell / f_r$ is evaluated. If $\hat{T}_{n_\ell}$ is above the thermal camera signal-to-noise ratio (SNR), then the heat has been transferred directly from one surface to the other, and the sheets are joined. In fact, $\hat{T}_{n_\ell}$ represents the frequency component at f_ℓ, which is the laser modulating frequency. Through data analysis and prior knowledge of equipment setup, $SNR = -33$dB has been chosen.

The following set is defined:

$$\mathcal{M} = \left\{ \begin{array}{r} (r, c) \in \mathbb{N}^2 : \hat{T}_{n_\ell}^{(r,c)} > SNR, n_\ell = N f_\ell / f_r, \\ r = 1, \ldots, H, \ c = 1, \ldots, W \end{array} \right\} \tag{12}$$

as the row and column frame indexes set corresponding to the joined points. For each point $(r, c) \in \mathcal{M}$, we evaluate the complex number $\tilde{T}_{n_\ell}$ phase

$$\angle \tilde{T}_{n_\ell} = \operatorname{atan2}\left(\mathbf{I}\left\{\tilde{T}_{n_\ell}\right\}, \mathbf{R}\left\{\tilde{T}_{n_\ell}\right\}\right), \tag{13}$$

where $\operatorname{atan2}(y, x) \in [-\pi, \pi]$ is the angle measure between the positive x-axis and the ray joining the origin to the cartesian point (x, y), and $\mathbf{R}(\cdot)$ and $\mathbf{I}(\cdot)$ are the argument real and imaginary part, respectively. The phase difference between distinct pixel signals represents a delay in the thermal signal diffusion. It is worth noting that the laser heat source moves at light speed; thus, it is applied to the tested surface simultaneously. Therefore, the signal delay (DFT phase difference) observed from the thermal camera is due to the internal structure of the welding point (thickness, nugget size, …).

It is worth noting that $\angle \tilde{T}_{n_\ell}$ in Eq. 13 is related to ϕ in Eq. 8. In fact, $\angle \tilde{T}_{n_\ell}$ represents the rear temperature delay from an arbitrary initial time instant. Thus, it is possible to write

$$\phi = \angle \tilde{T}_{n_\ell} - \phi_0, \tag{14}$$

where ϕ_0 is a constant value for all the points along the surface, accounting for the instant unknown laser activation time and the camera recording delay.

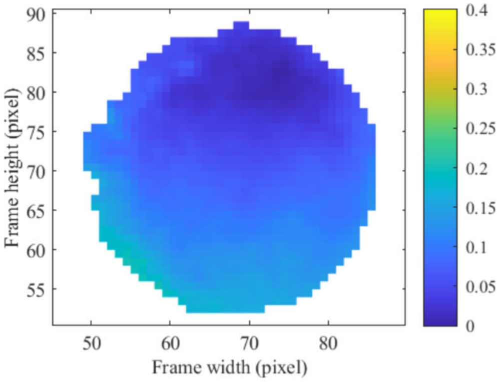

(a) 8.5 kA welded spot.

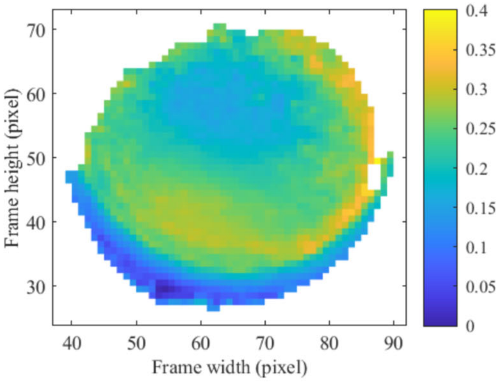

(b) 13 kA welded spot.

Fig. 8 Comparison of the DFT phase value map $\angle \tilde{T}_{n_\ell}^{(r,c)}, \forall (r, c) \in \mathcal{M}$ for a 8.5 kA and 13 kA welded spot. The 13 kA spot shows a larger phase variation, i.e., the color map is less uniform than the 8.5 kA spot

From $\angle \tilde{T}_{n_\ell}$, it is possible to evaluate the *through-plane* thermal diffusivity. In fact, from Eqs. 8 and 14, for each pixel, the following relation holds:

$$\frac{\angle \tilde{T}_{n_\ell} - \phi_0}{\ell} = \sqrt{\frac{\pi f_\ell}{D_s}}. \tag{15}$$

Using the presented set-up in transmission mode, only $\angle \tilde{T}_{n_\ell}$ is measurable, and f_ℓ is the known laser modulation frequency. Variations in the $\angle \tilde{T}_{n_\ell}$ values for different pixels highlight differences in the thickness ℓ and thermal diffusivity D_s along the surface, i.e., non-uniformities in the tested specimen.

Figure 8 compares the phase map computed for two distinct spots, one welded at 8.5 kA and at 13 kA. For the spot at 8.5 kA, the phase map is quite constant for a large part of the analyzed surface, leading to the conclusion that the internal section of the spot is uniform. On the other hand, the spot at 13 kA shows large phase variations due to some defects (e.g., thickness variations, as shown in Fig. 9c). To evaluate the variability in the phase map, we consider the phase variance computed as

$$v = \frac{1}{N_p - 1} \sum_{(r,c) \in \mathcal{M}} \left(\angle \tilde{T}_{n_\ell}^{(r,c)} - \mu\right)^2, \tag{16}$$

where

$$\mu = \frac{1}{N_p} \sum_{(r,c) \in \mathcal{M}} \angle \tilde{T}_{n_\ell}^{(r,c)} \tag{17}$$

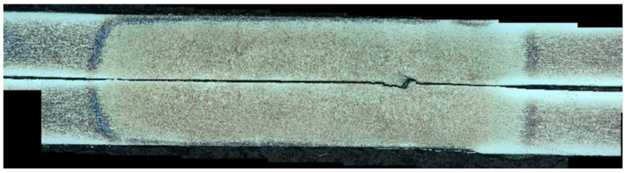

(a) 7.5 kA.

(b) 8.5 kA.

(c) 13 kA.

Fig. 9 Weld joint micrography comparison is the average phase along the considered surface, and $N_p = |\mathcal{M}|$ is the cardinality of the set $\mathcal{M}$.

3.4 Data interpretation

Thanks to the DFT processing described previously, some information from the active thermography analysis are achieved. In particular, the pixel map $\mathcal{M}$ and the phase variance index v.

Since $\mathcal{M}$ is the set of frame pixels where the weld spot is present, we estimate the spot area (in mm) as

$$\tilde{A} = \zeta^2 N_p \tag{18}$$

where ζ is the linear width of a pixel in mm. Note that we get the nugget diameter L from the weld inspection procedure. Thus, the nugget size must be estimated from the thermography experiment to validate the proposed approach. The following sets are defined:

$$\begin{aligned} \mathcal{R} &= \{r \in \mathbb{N} | \exists c \in \mathbb{N}, (r, c) \in \mathcal{M}\}, \\ \mathcal{C} &= \{c \in \mathbb{N} | \exists r \in \mathbb{N}, (r, c) \in \mathcal{M}\} \end{aligned} \tag{19}$$

as the sets of row and column indexes that appear at least once in $\mathcal{M}$. Since the specimens are cut along the frame width axis in the macrography analysis, the nugget diameter is estimated as

$$\begin{aligned} \tilde{L} = &\max_{r^* \in \mathcal{R}} \zeta\, (\overline{c} - \underline{c}) \\ &\text{s.t.} \\ &\overline{c} = \max_{c^* \in \mathcal{C},\ (r^*, c^*) \in \mathcal{M}} c^* \\ &\underline{c} = \min_{c^* \in \mathcal{C},\ (r^*, c^*) \in \mathcal{M}} c^* \end{aligned} \tag{20}$$

which is the maximum width of the pixel map $\mathcal{M}$.

However, the spot weld area only is not enough to evaluate the mechanical quality of the joint [56], since, e.g., the presence of expulsion [43], or microstructural changes [25, 44], may influence the mechanical properties.

4 Results

The specimens welded with a low current of 7.5 kA exhibited complete interfacial fractures. In contrast, the spots welded at 8.5 kA, and 13 kA with the presence of spatter, exhibited a pull-out fracture mode, as recommended by [3]. In the pull-out button, the fracture occurred either in the base metal or in the weld heat-affected zone at the perimeter of the weld. The failure occurred in the pullout mode for the expulsion-free samples, and the fracture was observed in the metal. However, for the samples experiencing expulsion, failure occurred either near the edge of the weld nugget or inside it.

The results of tensile tests and macrostructural joint analysis are summarized in Table 3. The specimens from series 1 have only half the ultimate tensile strength compared to those from series 2 and 3. These results highlight the importance of choosing appropriate welding parameters, such as the current intensity, to obtain a good quality joint.

The macrostructural analysis of the joint has been conducted, and the most significant images for each specimen class are presented in Fig. 9.

It is evident that the joint welded at 7.5 kA, from the micrograph in Fig. 9a, has no weld pool or nugget, highlighting that the two steel foils have not reached the fusion and they are only adhering each other. The HAZ and some microstructural changes are visible, with a small interface fracture. This joint is unacceptable even if inside the standard weldability parameter window.

An evident nugget and joining between the two parts are observed in the joint welded at 8.5 kA (see Fig. 9b). However, it seems that the electrode pressure has not been uniform across the joint, leading to an asymmetry that reflects in the thermal features.

Finally, the joint welded at 13 kA (see Fig. 9c) has a completely different geometry from the other two. The joint is significantly thinner due to the melting of a large amount of material. Moreover, the high temperature reached during the welding led to the melted material being evacuated, generating spatters.

The metallurgical analysis has been performed on 11 specimens from the three welding series. For these specimens, the measured nugget width L is compared to the estimated value $\tilde{L}$ from the thermography analysis Eq. 20 (see Fig. 10 and

Table 3 Tensile test results

Specimen set	Weld current (kA)	Failure mode	Peak load (kN)		Nugget diameter (mm)	
			Average	Standard deviation	Average	Standard deviation
1	7.5	IF	6774	1085	4.12	0.22
2	8.5	PO	11,231	692	5.57	0.73
3	13	PO	10,442	1419	6.04	0.12

Failure modes are interface fracture (*IF*) and pull-out mode (*PO*)

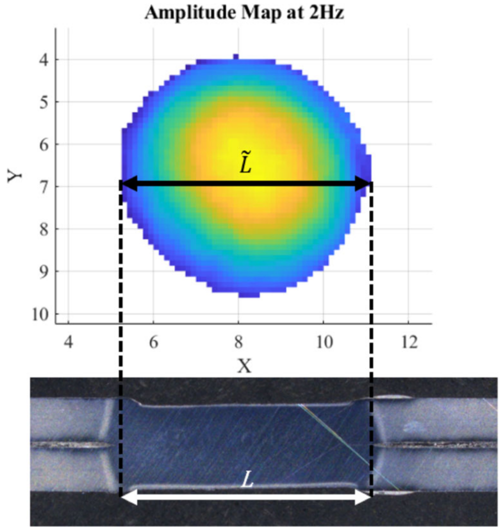

Fig. 10 Graphical representation of L and $\tilde{L}$ measurement

Fig. 11). The Pearson correlation coefficient between L and $\tilde{L}$ is

$$\rho = \frac{\sigma_{L,\tilde{L}}}{\sigma_L \sigma_{\tilde{L}}} = 0.9687, \tag{21}$$

highlighting the linear correlation between the two variables. Thus, the linear regression to relate $\tilde{L}$ to L is computed as

$$L = m\tilde{L} + q. \tag{22}$$

The parameter values $m = 0.9836$ and $q = -0.1762$ are estimated through the least-square fitting procedure. These results show good accuracy of the nugget size estimation from the thermography analysis. The results are close to the ideal condition, i.e., $m = 1$, $q = 0$. However, only 11 nuggets have been measured through metallurgical analysis. Moreover, through Eq. 20, we get the maximum nugget width from the thermography. On the other hand, the metallurgical analysis requires cutting the weld joint, leading to some uncertainty in preserving the maximum width. Since the estimated diameter size $\tilde{L}$ well approximates the measure L, we can consider the nugget area $\tilde{A}$ as an accurate estimation of the effective value.

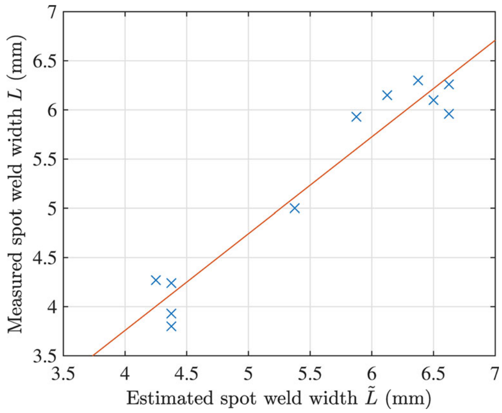

Fig. 11 Comparison of measured nugget width L measured from metallurgical and thermography analysis. The line represents the linear regression between L and $\tilde{L}$, and points are the measured values

The present study aims to evaluate the effectiveness of the thermographic method in assessing the spot weld quality. While the accuracy of the geometrical estimation results has been verified through the previously mentioned microstructural analysis, the mechanical properties are related to the joint internal properties. Thus, the thermographic analysis results, i.e., estimated nugget area and phase map variance, have been compared to the ultimate tensile strength (UTS). Since the geometrical nugget properties showed good accuracy, destructive testing has been performed to evaluate the UTS for the remaining 25 spots. The nugget area has been evaluated only by the thermographic analysis proposed in this paper for all the joints. The data interpolation procedure computed a UTS estimate value as a function of $\tilde{A}$ and v. In this study, we focus on classifying welding points as strong or weak, considering as threshold 80% the maximum acquired UTS (see, e.g., [39]).

Irregularities within the spot weld, frequent in the high-current generated specimens, lead to the decrease of the UTS, often under the chosen 80% threshold. Points in the weak region have small nugget areas corresponding to specimen set 1, with a low welding current. In this situation, we have observed homogenous nuggets identified by small phase variance values. On the other hand, the weak points in Fig. 12 are also the ones from specimen set 3, where the welding current is high (13 kA). In this third set, some points showed

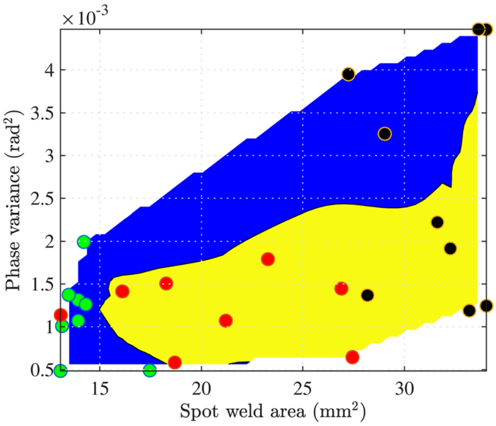

Fig. 12 Contour plot relating the spot weld area and phase variance to the joint quality. In blue is the area of the bad quality points, i.e., having UTS less than 80% of the maximum strength. In yellow is the area of the good quality points. The dot markers are the experimentally tested values from specimen sets 1 (green), 2 (red), and 3 (black)

low UTS values because material expulsion occurred during welding, leading to a non-uniform internal joint structure. This random behavior is well captured from the phase variance parameter v, whose value differs significantly across the specimens in set 3.

The acceptable weld points (i.e., within the yellow area in Fig. 12) are the ones with an estimated area larger than 15 mm and low phase variance. All the points from specimen set 2 fall into this category, and some from specimen set 3. In fact, it is worth noting that material expulsion is a random event that cannot be controlled in welding.

By looking at Fig. 12, it is clear that only the combination of weld area and phase variance from the thermographic testing accurately estimates the weld quality.

5 Conclusions

The present work introduces a novel methodology for non-destructive evaluation and testing resistance weld spots. This approach allows for assessing the nugget area and welds dis-homogeneity in a non-destructive manner. Moreover, the extracted features enable the evaluation of the mechanical properties of the joint. Notably, this methodology has the potential to be implemented for in-line testing of resistance spot welding (RSW), offering easy automation and enabling the classification of welded spots based on their area and variance, which provides valuable insights into the mechanical properties.

Future research endeavors will focus on expanding the scope of this study by increasing the number of specimens tested, exploring a broader range of weld parameters such as pressure, current, and welding time, and investigating various thicknesses and materials. These extensions will further enhance our understanding of the proposed methodology and its applicability in practical welding scenarios.

Funding This study was supported by J-Tech@PoliTO, an advanced joining technologies research center at Politecnico di Torino (https://www.j-tech.polito.it/).

Declarations

Conflict of interest The authors declare a potential competing interest related to this work. The subject matter of this manuscript is covered under the patent application no. 102023000023949 filed by the Politecnico di Torino.

References

1. Allen RL, Mills DW (2004) Signal analysis: time, frequency, scale, and structure. John Wiley & Sons. https://doi.org/10.1002/047166037X
2. AWS (2013) D8.1M:2013 - Specification for automotive weld quality - resistance spot welding of steel
3. AWS (2019). C1.1M/C1.1:2019 - Recommended practices for resistance welding
4. AWS (2022) D8.9M:2022 - Test methods for evaluating the resistance spot welding behavior of automotive sheet steel materials
5. Bagavathiappan S, Lahiri B, Saravanan T, Philip J, Jayakumar T (2013) Infrared thermography for condition monitoring - a review. Infrared Phys Technol 60:35–55. https://doi.org/10.1016/j.infrared.2013.03.006
6. Bang HT, Park S, Jeon H (2020) Defect identification in composite materials via thermography and deep learning techniques. Compos Struct 246:112405. https://doi.org/10.1016/j.compstruct.2020.112405
7. Broberg P (2013) Surface crack detection in welds using thermography. NDT E Int 57:69–73. https://doi.org/10.1016/j.ndteint.2013.03.008
8. Cantini L, Cucchi M, Fava G, Poggi C, (2012) Fourier analysis applied to infrared thermography of fiber composites used for the strengthening of structural elements. In: Proceedings of the 11th international conference on quantitative infrared thermography. QIRT Council, pp 1–9. https://doi.org/10.21611/qirt.2012.392
9. Cheng Y, Bai L, Yang F, Chen Y, Jiang S, Yin C (2016) Stainless steel weld defect detection using pulsed inductive thermography. IEEE Trans Appl Supercond 26:1–4. https://doi.org/10.1109/TASC.2016.2582662
10. Cifuentes Á, Mendioroz A, Salazar A (2017) Simultaneous measurements of the thermal diffusivity and conductivity of thermal insulators using lock-in infrared thermography. Int J Therm Sci 121:305–312. https://doi.org/10.1016/j.ijthermalsci.2017.07.023
11. Da Silva WF, Melo RAC, Grosso M, Pereira GR, Riffel DB (2020) Active thermography data-processing algorithm for nondestructive testing of materials. IEEE Access 8:175054–175062. https://doi.org/10.1109/ACCESS.2020.3025329
12. Dahmene F, Yaacoubi S, Mahjoub EM, Bouzenad AE, Rabaey P, Masmoudi M, Nennig P, Dupuy T, Benlatreche Y, Taram A (2022) On the nondestructive testing and monitoring of cracks in resistance spot welds: recent gained experience. Weld World 66:629–641. https://doi.org/10.1007/s40194-022-01249-w
13. Dell'Avvocato G, Gohlke D, Palumbo D, Krankenhagen R, Galietti U (2022) Quantitative evaluation of the welded area in resistance projection welded (RPW) thin joints by pulsed laser thermography. In: Mendioroz A, Avdelidis NP (eds) Thermosense: thermal infrared applications XLIV, International Society for Optics and Photonics. SPIE pp 121090J. https://doi.org/10.1117/12.2618806
14. Dell'Avvocato G, Palumbo D, Palmieri ME, Galietti U, (2022) Non-destructive thermographic method for the assessment of heat treatment in boron steel. In: Mendioroz A, Avdelidis NP (eds) Thermosense: thermal infrared applications XLIV, International Society for Optics and Photonics.SPIE pp 1210906. https://doi.org/10.1117/12.2618810
15. Doshvarpassand S, Wu C, Wang X (2019) An overview of corrosion defect characterization using active infrared thermography. Infrared Phys Technol 96:366–389. https://doi.org/10.1016/j.infrared.2018.12.006
16. García de la Yedra A, Fernández E, Beizama A, Fuente R, Echeverria A, Broberg P, Runnemalm A, Henrikson P (2014) Defect detection strategies in nickel superalloys welds using active thermography. In: Proceedings of the 12th international conference on quantitative infrared thermography, QIRT Council pp 1–8. https://doi.org/10.21611/qirt.2014.028
17. Grys S, Vokorokos L, Borowik L (2014) Size determination of subsurface defect by active thermography - simulation research. Infrared Phys Technol 62:147–153. https://doi.org/10.1016/j.infrared.2013.11.011

18. Guo X, Vavilov V (2013) Crack detection in aluminum parts by using ultrasound-excited infrared thermography. Infrared Phys Technol 61:149–156. https://doi.org/10.1016/j.infrared.2013.08.003
19. Hagqvist P, Sikström F, Christiansson AK, Lennartson B (2014) Emissivity compensated spectral pyrometry for varying emissivity metallic measurands. Meas Sci Technol 25:025010. https://doi.org/10.1088/0957-0233/25/2/025010
20. Honner M, Litoš P, Švantner M (2004) Thermography analyses of the hole-drilling residual stress measuring technique. Infrared Phys Technol 45:131–142. https://doi.org/10.1016/j.infrared.2003.08.001
21. Huang J, Pastor M, Garnier C, Gong X (2019) A new model for fatigue life prediction based on infrared thermography and degradation process for CFRP composite laminates. Int J Fatigue 120:87–95. https://doi.org/10.1016/j.ijfatigue.2018.11.002
22. Huang KL, Sfarra S, Wen CM, Yao Y, Zhao C (2021) Exploratory factor analysis for defect identification with active thermography. Meas Sci Technol 32:114010. https://doi.org/10.1088/1361-6501/ac17f9
23. Hussein KM, Akbari H, Noorossana R, Yadegari R, Ashiri R (2023) Mechanical behavior investigation for quenching and partitioning steel dissimilar resistance spot welds. J Mater Res Technol 27:4064–4073. https://doi.org/10.1016/j.jmrt.2023.10.220
24. ISO Central Secretary (2021) Resistance welding - Vocabulary - Part 1: Spot, projection and seam welding. Standard BS EN ISO 17677-1:2021. International Organization for Standardization. Geneva, CH
25. Javaheri E, Lubritz J, Graf B, Rethmeier M (2020) Mechanical properties characterization of welded automotive steels. Metals 10:1. https://doi.org/10.3390/met10010001
26. Jonietz F, Myrach P, Suwala H, Ziegler M (2015) Examination of spot welded joints with active thermography. J Nondestruct Eval 35:1. https://doi.org/10.1007/s10921-015-0318-4
27. Kassam S, Poor H (1985) Robust techniques for signal processing: a survey. Proc IEEE 73:433–481. https://doi.org/10.1109/PROC.1985.13167
28. Kato H, Baba T, Okaji M (2001) Anisotropic thermal-diffusivity measurements by a new laser-spot-heating technique. Meas Sci Technol 12:2074. https://doi.org/10.1088/0957-0233/12/12/307
29. Li T, Almond DP, Rees DAS (2011) Crack imaging by scanning pulsed laser spot thermography. NDT E Int 44:216–225. https://doi.org/10.1016/j.ndteint.2010.08.006
30. Li W (2004) Modeling and on-line estimation of electrode wear in resistance spot welding. J Manuf Sci Eng 127:709–717. https://doi.org/10.1115/1.2034516
31. Maierhofer C, Myrach P, Krankenhagen R, Röllig M, Steinfurth H (2015) Detection and characterization of defects in isotropic and anisotropic structures using lock-in thermography. J Imaging 1:220–248. https://doi.org/10.3390/jimaging1010220
32. Maierhofer C, Röllig M, Steinfurth H, Ziegler M, Kreutzbruck M, Scheuerlein C, Heck S (2012) Non-destructive testing of Cu solder connections using active thermography. NDT E Int 52:103–111. https://doi.org/10.1016/j.ndteint.2012.07.010
33. Martín Ó, Pereda M, Santos JI, Galán JM (2014) Assessment of resistance spot welding quality based on ultrasonic testing and tree-based techniques. J Mater Process Technol 214:2478–2487. https://doi.org/10.1016/j.jmatprotec.2014.05.021
34. Mendioroz A, Fuente-Dacal R, Apiñaniz E, Salazar A (2009) Thermal diffusivity measurements of thin plates and filaments using lock-in thermography. Rev Sci Instrum 80:074904. https://doi.org/10.1063/1.3176467
35. Meng X, Wang Y, Liu J, He W (2019) Nondestructive inspection of curved clad composites with subsurface defects by combination active thermography and three-dimensional (3D) structural optical imaging. Infrared Phys Technol 97:424–431. https://doi.org/10.1016/j.infrared.2019.01.026
36. Misokefalou E, Papoutsidakis M, Priniotakis G (2022) Non-destructive testing for quality control in automotive industry. Int J Eng Appl Sci Technol 7:349–355. https://doi.org/10.33564/ijeast.2022.v07i01.054
37. Paoloni S, Tata ME, Scudieri F, Mercuri F, Marinelli M, Zammit U (2010) IR thermography characterization of residual stress in plastically deformed metallic components. Appl Phys A 98:461–465. https://doi.org/10.1007/s00339-009-5422-9
38. Park H, Choi M, Park J, Kim W (2014) A study on detection of micro-cracks in the dissimilar metal weld through ultrasound infrared thermography. Infrared Phys Technol 62:124–131. https://doi.org/10.1016/j.infrared.2013.10.006
39. Peng J, Fukumoto S, Brown L, Zhou N (2004) Image analysis of electrode degradation in resistance spot welding of aluminium. Sci Technol Weld Join 9:331–336. https://doi.org/10.1179/136217104225012256
40. Philipp A, Pech-May NW, Kopera BAF, Lechner AM, Rosenfeldt S, Retsch M (2019) Direct measurement of the in-plane thermal diffusivity of semitransparent thin films by lock-in thermography: an extension of the slopes method. Analytical Chemistry 91:8476–8483. https://doi.org/10.1021/acs.analchem.9b01583
41. Pitarresi G, Cappello R, Capraro A, Pinto V, Badagliacco D, Valenza A (2023) Frequency modulated thermography-NDT of polymer composites by means of human-controlled heat modulation. In: Rizzo P, Milazzo A (eds) European workshop on structural health monitoring.Springer International Publishing pp 610–618. https://doi.org/10.1007/978-3-031-07258-1_62
42. Pouranvari M (2011) Effect of welding parameters on the peak load and energy absorption of low-carbon steel resistance spot welds. ISRN Mech Eng 2011:824149. https://doi.org/10.5402/2011/824149
43. Pouranvari M, Abedi A, Marashi P, Goodarzi M (2008) Effect of expulsion on peak load and energy absorption of low carbon steel resistance spot welds. Sci Technol Weld Join 13:39–43. https://doi.org/10.1179/174329307X249342
44. Rajarajan C, Sonar T, Sivaraj P, Raja S, Mathiazhagan N (2022) Investigating the effect of electrode pressure on nugget size, microstructure and tensile shear strength of resistance spot welded advanced high strength dual phase steel joints. Metallogr Microstruct Anal 11:472–483. https://doi.org/10.1007/s13632-022-00862-x
45. Rajic N (2002) Principal component thermography for flaw contrast enhancement and flaw depth characterisation in composite structures. Compos Struct 58:521–528. https://doi.org/10.1016/S0263-8223(02)00161-7
46. Rajic N, Antolis C (2017) An investigation of noise performance in optical lock-in thermography. Infrared Phys Technol 87:1–10. https://doi.org/10.1016/j.infrared.2017.09.019
47. Runnemalm A, Ahlberg J, Appelgren A, Sjökvist S (2014) Automatic inspection of spot welds by thermography. J Nondestruct Eval 33:398–406. https://doi.org/10.1007/s10921-014-0233-0
48. Sadiq H, Wong MB, Tashan J, Al-Mahaidi R, Zhao XL (2013) Determination of steel emissivity for the temperature prediction of structural steel members in fire. J Mater Civ Eng 25:167–173. https://doi.org/10.1061/(ASCE)MT.1943-5533.0000607
49. Santoro L, Sesana R, Molica Nardo R, Curá F (2023) Infrared in-line monitoring of flaws in steel welded joints: a preliminary approach with SMAW and GMAW processes. Int J Adv Manuf Technol. https://doi.org/10.1007/s00170-023-12044-2
50. Schlichting J, Brauser S, Pepke LA, Maierhofer C, Rethmeier M, Kreutzbruck M (2012) Thermographic testing of spot welds. NDT E Int 48:23–29. https://doi.org/10.1016/j.ndteint.2012.02.003
51. Sesana R, Santoro L, Curà F, Molica Nardo R, Pagano P (2023) Assessing thermal properties of multipass weld beads using active

thermography: microstructural variations and anisotropy analysis. Int J Adv Manuf Technol. https://doi.org/10.1007/s00170-023-11951-8

52. Sirikham A, Zhao Y, Liu H, Xu Y, Williams S, Mehnen J (2020) Three-dimensional subsurface defect shape reconstruction and visualisation by pulsed thermography. Infrared Phys Technol 104:103151. https://doi.org/10.1016/j.infrared.2019.103151
53. Song J, Gao B, Woo W, Tian G (2020) Ensemble tensor decomposition for infrared thermography cracks detection system. Infrared Phys Technol 105:103203. https://doi.org/10.1016/j.infrared.2020.103203
54. Srajbr C (2016) Induction excited thermography in industrial applications. In: Proceedings of 19th World Conference on Non-Destructive Testing (WCNDT 2016), pp 1–9
55. Strzałkowski K, Streza M, Dadarlat D, Marasek A (2015) Thermal characterization of II-VI binary crystals by photopyroelectric calorimetry and infrared lock-in thermography. J Therm Anal Calorim 119:319–327. https://doi.org/10.1007/s10973-014-4137-0
56. Summerville C, Compston P, Doolan M (2019) A comparison of resistance spot weld quality assessment techniques. Procedia Manuf 29:305–312. https://doi.org/10.1016/j.promfg.2019.02.142. “18th International Conference on Sheet Metal, SHEMET 2019” “New Trends and Developments in Sheet Metal Processing”
57. Susa M, Maldague X, Svaic S, Boras I, Bendada A (2008) The influence of surface coatings on the differences between numerical and experimental results for samples subject to a pulse thermography examination. In: Proceedings of the 9th international conference on quantitative infrared thermography. QIRT Council pp 1–8. https://doi.org/10.21611/qirt.2008.12_11_16
58. Yuan B, Spiessberger C, Waag TI (2017) Eddy current thermography imaging for condition-based maintenance of overlay welded components under multi-degradation. Mar Struct 53:136–147. https://doi.org/10.1016/j.marstruc.2017.02.001
59. Zhang X, Chen G, Zhang Y (2008) Characteristics of electrode wear in resistance spot welding dual-phase steels. Mater Des 29:279–283. https://doi.org/10.1016/j.matdes.2006.10.025
60. Zhou K, Yao P (2019) Overview of recent advances of process analysis and quality control in resistance spot welding. Mech Syst Signal Process 124:170–198. https://doi.org/10.1016/j.ymssp.2019.01.041
61. Zhou Q, Rong Y, Shao X, Jiang P, Gao Z, Cao L (2018) Optimization of laser brazing onto galvanized steel based on ensemble of metamodels. J Intell Manuf 29:1417–1431. https://doi.org/10.1007/s10845-015-1187-5